JOURNAL OF MATERIALS SCIENCE 25 (1990) 4866–4872

Microstructure and mechanical properties of sintered glass

L. CORONEL, J. P. JERNOT, F. OSTERSTOCK
LERMAT – ISMRa, Ura 1317, 14032 Caen Cedex, France

Glass microspheres have been sintered under argon in order to obtain sintered brittle bodies over a large range of density. During sintering, the microstructure evolves from a stacking of spheres to a body containing isolated pores. This evolution of the microstructure is described using image analysis and mathematical morphology. Mechanical properties are also investigated as a function of density. Special attention was paid to fracture toughness because, due to the isotropic behaviour of glass, internal stresses of the second order do not exist. A maximum of G_{IC} is observed and it can be correlated with changes in the morphological parameters.

1. Introduction

The mechanical behaviour of brittle porous materials becomes important especially in the case of fine ceramics. Due to the kind of application or the conditions of use, porosity is induced either during fabrication in order to enhance the thermal shock resistance, or may result from thermal shock as microcracks or from creep as cavities. Thus the remaining resistance of ceramic structural parts depends on their thermomechanical history.

In the case of the rupture stress and toughness values, mostly empirical laws have been proposed. This is because in the case of polycrystalline ceramics the influence of both internal stresses of the second order, impurities and porosity is difficult to take into account. As an example, the experimental results of Evans and Tappin [1] and those of Pabst [2] used in the geometrical model of Rice *et al.* [3, 4] seem to be contradictory.

In this respect sintered glass appears to be an ideal material able to yield phenomenological laws for such problems.

2. Material and experimental procedure

2.1. Powder

The powder used is a commercial powder, Blastoline 70-100, (Vestglass, West Germany). A micrograph of the powder is presented in Fig. 1. The size distribution was determined by image analysis and a mean value of 100 μm was obtained. A histogram and a cumulative curve of the size distribution are shown in Fig. 2. The apparent density and the tap density of this spherical powder are, respectively, 1.44 and 1.58, corresponding to volume fractions 0.58 and 0.63.

2.2. Sintering

The glass powder was introduced into graphite crucibles and tapped to settle the powder. Sintering was carried out in a Sedimmec furnace under argon at temperatures between 650 and 700° C for periods of 1 to 27 h. Discs ($\sim$ 15 mm diameter $\times$ 4 mm) and elongated platelets ($\sim$ 45 mm $\times$ 4 mm $\times$ 8 mm) were obtained in order to determine microstructural and mechanical properties.

2.3. Image analysis

The discs were impregnated under vacuum with an epoxy resin for metallographic purposes. The best results were obtained after polishing for a short time with abrasive papers (grades 600 and 1200) followed by a cloth impregnated with diamond paste (6 μm). In this way, the glass was polished and not the resin, giving a good contrast for optical microscopy.

A Leitz texture analyser was used to determine the microstructural properties of the sample (the phase of interest being detected, digitized and stored in the computer's memory for analysis). The main stereological parameters accessible on the polished sections are: the volumic fraction of the solid phase, $V_v(S)$; the specific surface area of the solid/pore interface, $S_v(S/P)$; the integral of mean curvature of the solid/pore interface, $M_v(S/P)$. The mean value of the mean curvature of the solid/pore interface, H, is accessible from the last two parameters using the relation [5]

$$\bar{H} = \frac{M_v}{S_v} \quad (1)$$

Other important parameters can be obtained using mathematical morphology [6, 7]. Among them, the star function derived from the $P(l)$ function (corresponding to the probability for a segment of length l to be included in the phase of interest) is of particular importance for sintered materials [8, 9]. The star function in three-dimensional space allows definition of a kind of mean free volume in a phase (the corresponding star function in one-dimensional space – linear analysis – defines in the phase a mean free path weighted in measure). [6]

0022–2461/90 $03.00 + .12

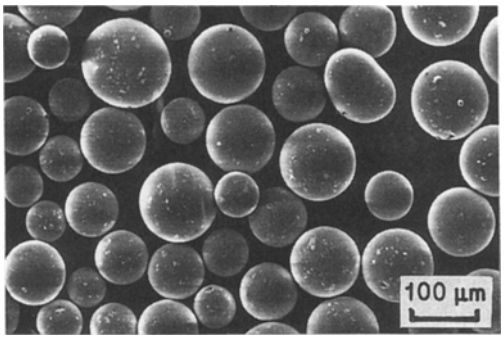

Figure 1 Micrograph of the glass powder.

2.4. Mechanical testing

The platelets were prepared for mechanical characterization and fractography. It was aimed to size the specimens and to remove the outer skin and the possibly associated thermal residual stresses. Mechanical testing was performed in three-point bending using a Schenck-Trebel (100 RMC) universal testing machine. Young's modulus, E, and rupture stress, σ_r, were calculated using the expressions derived from continuum mechanics, i.e.

$$E = \frac{F}{h}\left(\frac{L^3}{4bW^3}\right) \quad (2)$$

$$\sigma_r = F_r\left(\frac{3L}{2bW^2}\right) \quad (3)$$

where F is the applied load, h the displacement corresponding to F in the elastic domain, and F_r the maximum load at rupture. Other parameters are as defined in Fig. 3.

The dynamic Young's modulus measurements were made at IWW-TU Clausthal (West Germany) using the resonance method.

The critical stress intensity factor, K_{IC}, was calculated using

$$K_{IC} = \sigma_r Y a^{1/2} \quad (4)$$

where a is the length of the introduced notch, and Y a geometrical factor

$$Y = 1.93 - 3.07\left(\frac{a}{W}\right) + 14.53\left(\frac{a}{W}\right)^2 - 25.11\left(\frac{a}{W}\right)^3 + 25.80\left(\frac{a}{W}\right)^4 \quad (5)$$

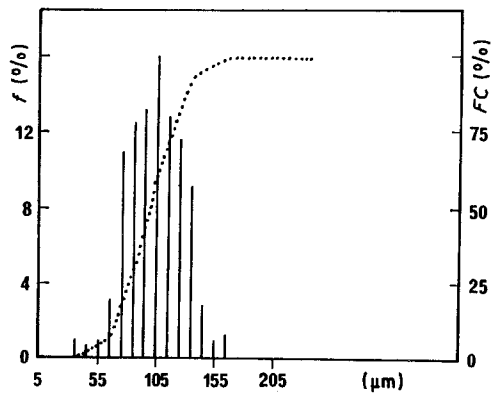

Figure 2 Size distribution of the powder determined by image analysis.

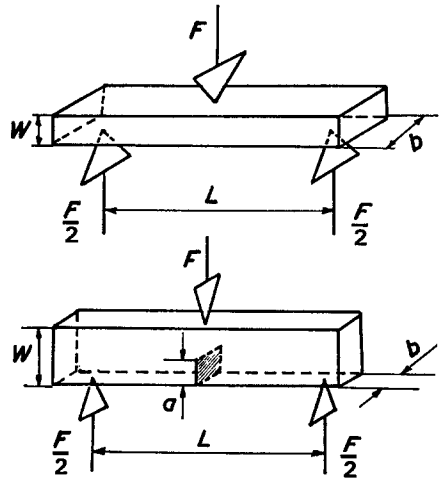

Figure 3 Characteristics of the samples used for mechanical testing.

Observations were made after controlled crack propagation or after rupture within a scanning electron microscope, Jeol JMS-T330 A.

Notches were introduced using copper blades of 50 µm thickness with deposited diamond powder. A resulting notch in a sample with 27% porosity is shown in Fig. 4; the shape and root radius of the notches remained constant over the whole density range.

3. Experimental results

3.1. Microstructure

The micrographs in Fig. 5 show different steps of the densification of the powder during sintering (the black phase corresponds to the pores and the white one to the glass). Basically, the microstructural evolution is similar to solid phase sintering of metallic powders [10].

The evolution of the volumic fraction of the solid phase, $V_v(S)$, for isothermal sintering is represented in Fig. 6. The mechanism of densification is the viscous flow and the transition from low densification rate to high densification rate occurs over a narrow range of temperatures (650 to 700° C).

Among the stereological parameters, the specific surface of the pore/solid interface (not represented here) decreases regularly as a function of $V_v(S)$, when sintering progresses. On the contrary, evolution of the average mean surface curvature, H, is much less regular (Fig. 7) and the different steps of sintering can

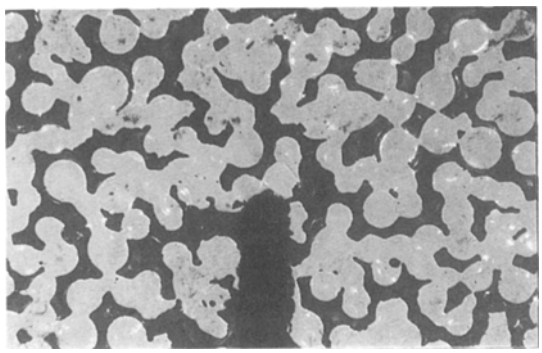

Figure 4 Optical micrograph of a notched specimen.

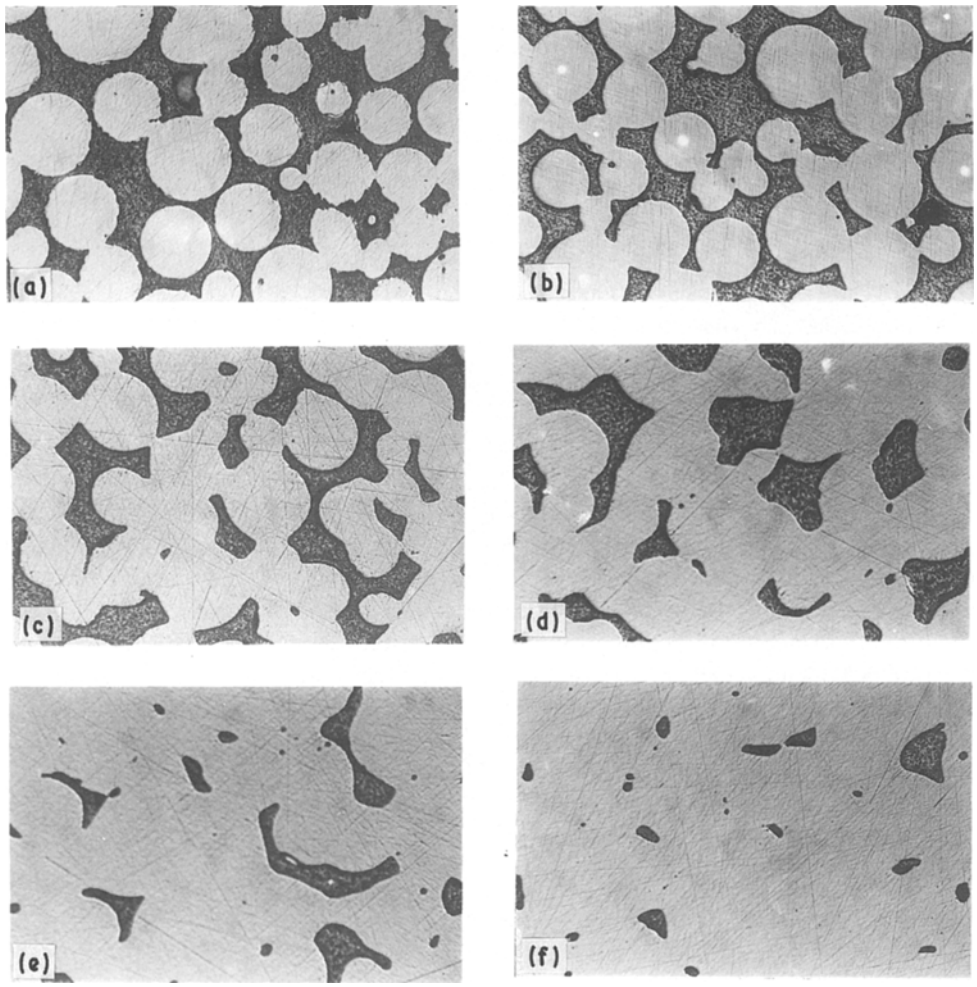

Figure 5 Microstructural evolution of the glass powder.

be recognized [11]. Up to a volume fraction $V_v(S) \simeq 0.7$ to 0.8 the decrease in the curvature is linked to the creation and growth of necks between the particles. After this step, further reduction of the curvature can be linked to the closure of the channels. At the very end of sintering, the curvature will increase towards zero with progressive elimination of the pores.

This quantitative description of the microstructure can be completed efficiently with another parameter accessible from mathematical morphology: the star function in the three-dimensional space. The evolution of this parameter measured for the solid phase is presented in Fig. 8. It can be seen that its value is low at the beginning, corresponding roughly to the volume of the particles. Above the range $V_v(S) \simeq 0.7$ to 0.8, it increases abruptly with the coalescence of the particles.

3.2. Mechanical properties

3.2.1. Young's modulus

The variation of E with the volume fraction of the solid phase is shown in Fig. 9. At lower densities

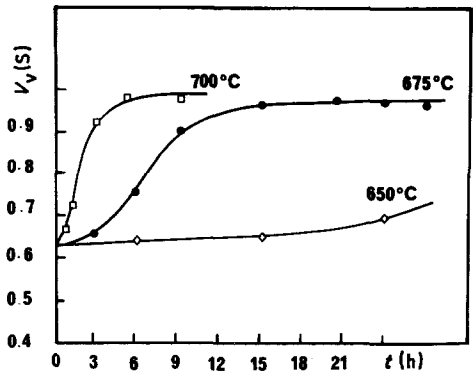

Figure 6 Densification of the powder by isothermal sintering.

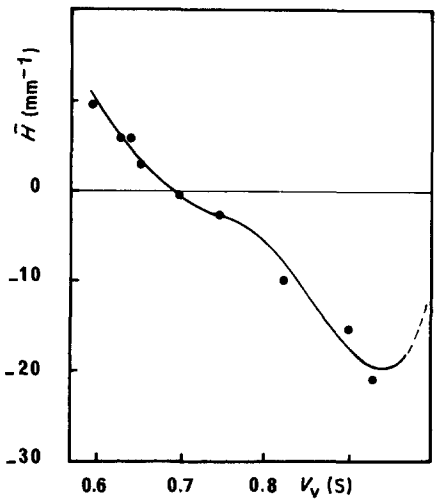

Figure 7 Average mean surface curvature as a function of relative density.

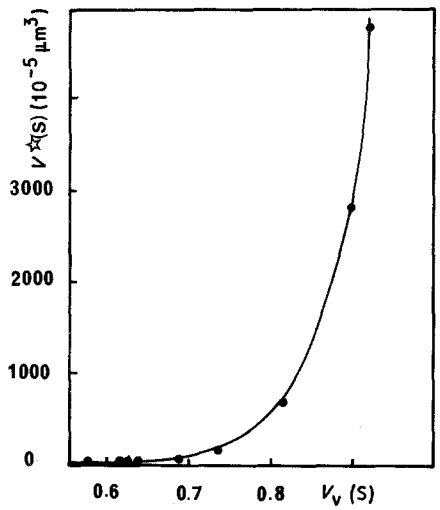

Figure 8 Evolution of the star function in the solid phase.

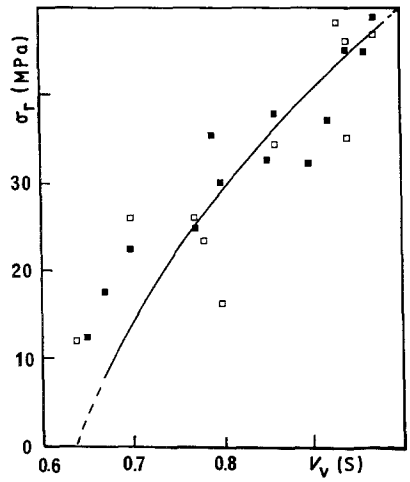

Figure 10 Variation of rupture stress with relative density. (■) 300 μm min^{-1}, (□) 30 μm min^{-1}.

($< 70\%$), the resonance method could not be used, and only static values are available. Both static (open points) and dynamic values (solid points) may be described by the same curve. As usual, the Young's modulus tends towards zero as the density of the sintered body tends towards the density of the initial powder.

3.2.2. Rupture stress

The values are plotted as a function of density in Fig. 10. The measurements were run at two cross-head speeds in order to take into account possible stress corrosion effects. The scattering is rather large but the values can be roughly described by a single curve.

3.2.3. Fracture toughness

The shape of the load–displacement curve depends on the density. Two examples are replotted in Fig. 11. Crack propagation was catastrophic in materials with high density and stable in those with low densities. In all cases, the critical stress intensity factor was calculated from the maximum load. The tests were run at a cross-head speed such that the maximum load was reached within 10 sec. This was also the time to rupture of the unnotched specimens at a cross-head speed of 300 μm min^{-1}.

First observation of the fracture surface showed that crack propagation occurred in mode I. Fig. 12 shows the variation of the critical stress intensity factor, K_{IC}, with density. A continuous decrease towards zero at the initial powder density is observed. The open points (density near the bulk) represent values which are not valid because the notch root radius was not sharp enough [12, 13]. They have thus been ignored. In all three cases (σ_r, E and K_{IC}), the extrapolation of experimental points to full density yields a value corresponding to the bulk.

Calculating the critical strain energy release rate, G_{IC}, using Irwin's relationship and the Young modulus of each sample, yields the plot in Fig. 13. On the contrary to K_{IC}, G_{IC} exhibits a maximum near a relative density ~ 0.75.

4. Discussion

The main observation which can be made from the experimental results is that G_{IC} exhibits a maximum value when it is plotted as a function of density (Fig. 13). This behaviour can be confirmed by the comparison of areas under the load–displacement curves in Fig. 11. This variation of G_{IC} does not follow the classical variation of physical properties of sintered materials. Usually, a regular increase towards

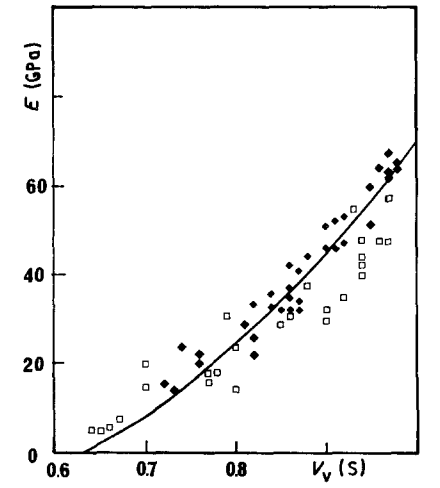

Figure 9 Variation of Young's modulus with relative density. (◆) dynamic, (□) static.

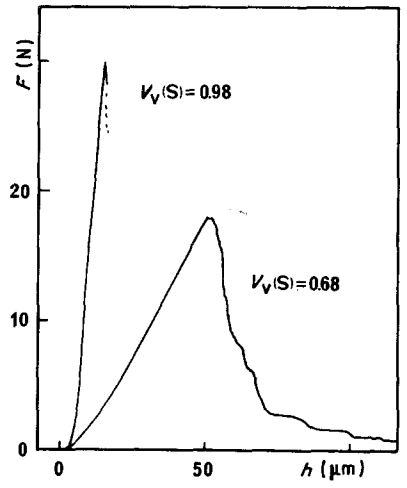

Figure 11 Load–displacement curves for two samples with different relative densities.

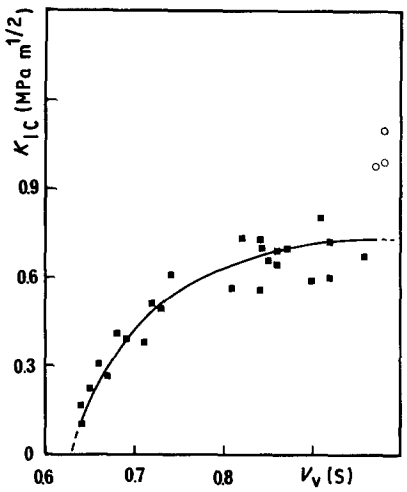

Figure 12 Variation of K_{IC} with relative density.

the property value of the bulk is observed as sintering progresses. This usual behaviour can be found in Figs 9 and 10 for Young's modulus, E, and rupture stress, σ_r.

Physical properties, such as Young's modulus, electrical conductivity or rupture stress, can be described by taking into account the volumic fraction of the solid phase, i.e. the quantity of matter [14–16]. More refined models making use of the size of the necks [17] or the load-bearing area [18, 19] can be found in the literature. All these descriptions show a regular increase of the properties with density: none of them predicts a maximum.

In variance with other properties, G_{IC} is not a volume property but it deals with a creation of surfaces. In this respect, a model was proposed by Rice and Freiman [3]. They based their derivation on the assumptions of Knudsen [20] using the shortest fracture path concept (see Fig. 14). Their work yields an exponential decrease of G_{IC} with increasing porosity. This does neither fit the results of Fig. 13. In fact, they used G_{IC} as a quantity and multiplied it by the relative fracture area. Thus, two basic points are missing.

Firstly, G_{IC} is not a quantity of energy but an energy rate [21, 22]. Secondly the influence of the micromechanisms of crack front pinning and crack deflection on G_{IC} of the bulk material are not taken into

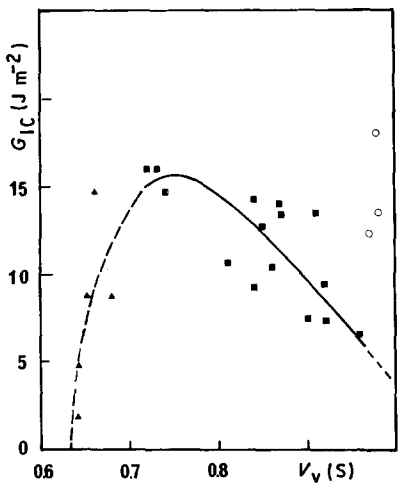

Figure 13 Variation of G_{IC} with relative density.

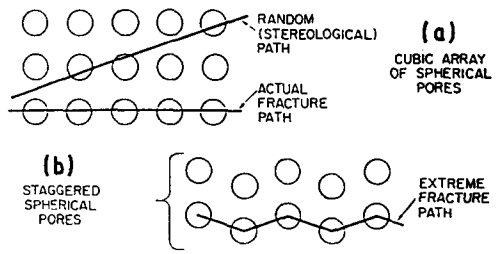

Figure 14 Illustration of the shortest fracture path concept (from Rice and Freiman [3]).

account. In other words, it is assumed that the crack propagation in the solid phase occurs at the same value of G_{IC} as porosity varies. Indeed, the contribution of all these micromechanisms and the way they are influenced by the microstructure is very difficult to describe.

In addition, as can be seen in Fig. 5, discussion of a single microstructure has little physical meaning. The different steps of sintering lead to large changes in the morphology of the sintered body. These changes corresponding to the successive steps of sintering can be followed quantitatively with the mean value of the mean curvature of the pore/solid interface, $\bar{H}$, reported in Fig. 7 [11]. At the beginning of sintering, the positive radii or curvature of the particles are linked to the positive values of $\bar{H}$. Then, concave surfaces appear with the creation and growth of necks: $\bar{H}$ decreases rapidly. A further increase in the size of the necks does not affect appreciably the whole curvature and the rate of diminution of $\bar{H}$ falls. As the sintering progresses, the closure of the channels created in the porous body brings new concave surfaces to the structure and $\bar{H}$ decreases again abruptly. After this step, coalescence and elimination of the pores leads to an increase in $\bar{H}$ towards zero at the end of the sintering. The step of closure of the channels corresponding to a coalescence of the particulate structure is confirmed by the evolution of the star function, $V^*(S)$, of the solid phase (see Fig. 8). From a relative density ~ 0.75 the mean free path in the solid phase increases considerably.

Schematically, two types of structures can be distinguished: (i) At low densities, a particulate structure is observed. Its resistance stems from the contacts (number and size) between the particles and the multiple interactions between the rows of particles as can be observed in a granular medium [23]. Moreover, the growth of the necks increases the load-bearing area. (ii) At high densities, the microstructure can be described as a bulk containing pores.

These two structures interact in a different way with the stress field, as can be seen in Figs 15 and 16. This distinction between the two microstructures may help to describe the behaviour of G_{IC} in terms of two increases. At low densities the strengthening of the structure associated with the growth of necks leads to an increase of G_{IC}. At high densities the augmentation of porosity induces more and more obstacles to crack propagation (crack pinning and crack deflection). These two reinforcement mechanisms meet roughly at a relative density $\simeq 0.75$ and correspond to the transition between the two limiting microstructures.

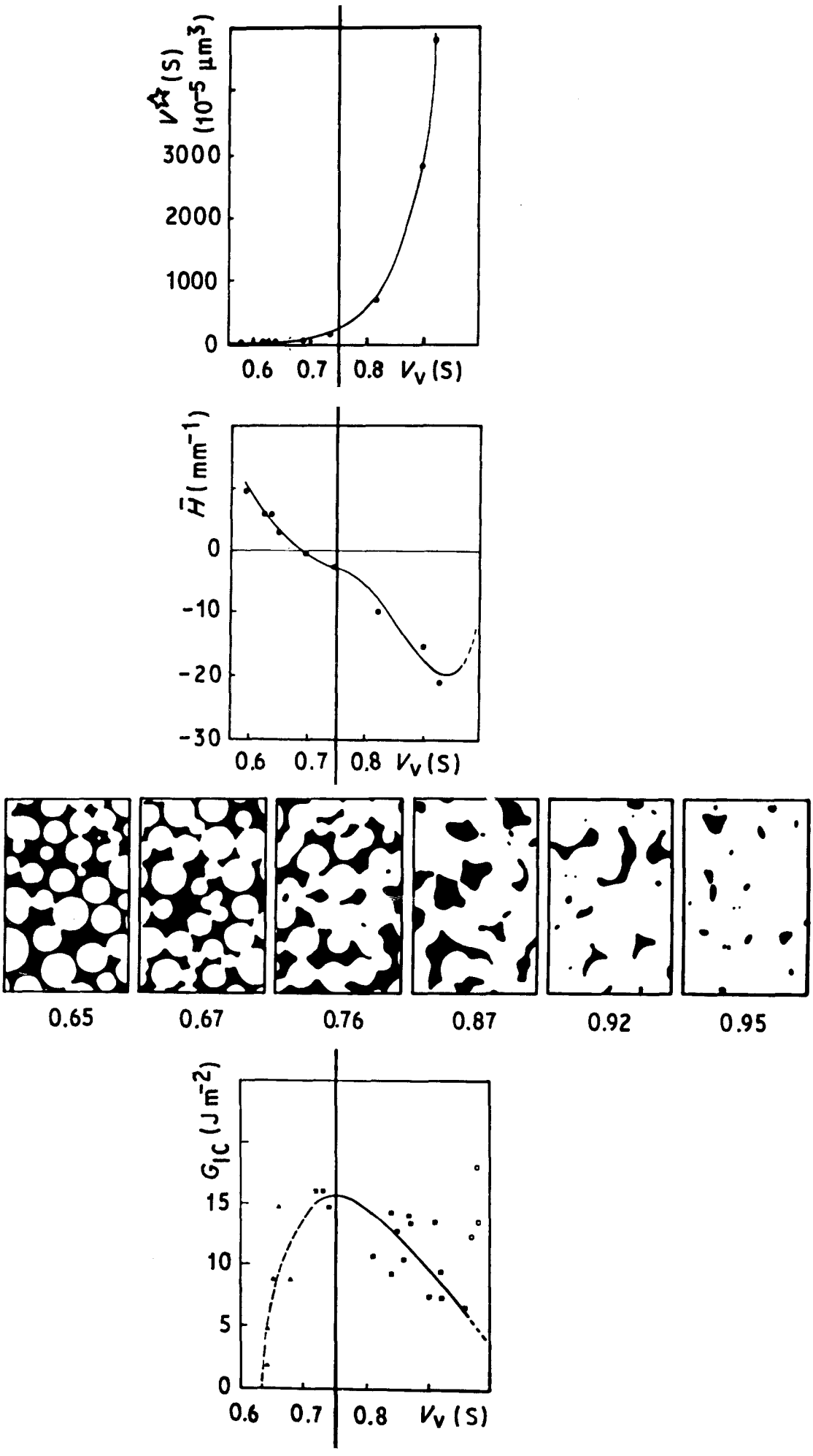

Figure 15 Similarities between the microstructural and the mechanical behaviour.

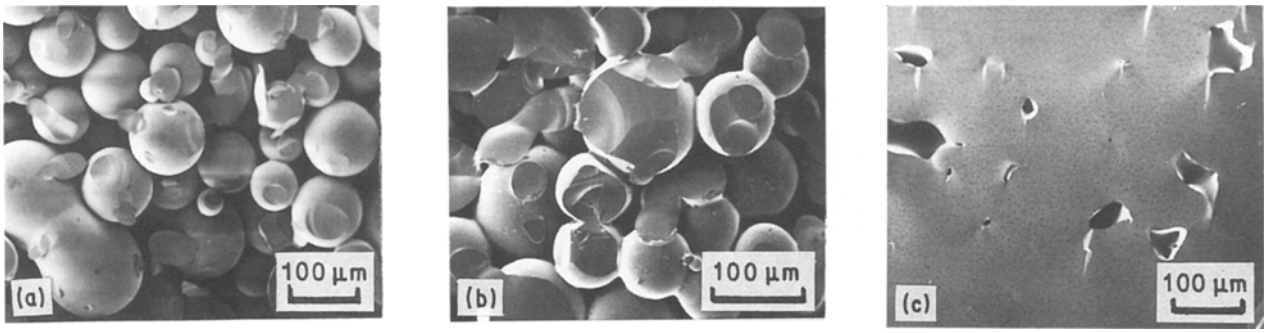

Figure 16 Fracture surface of three samples with increasing relative densities.

5. Conclusion

All but one of the measured properties of sintered glass evolve as usually observed on sintered materials. The critical strain energy release rate, G_{IC}, exhibits a peculiar behaviour: its evolution passes through a maximum as density increases. This surprising behaviour can be qualitatively correlated with the morphology of the sintered glass. Two limiting microstructures can be considered: particulate at low densities and porous bulk at high densities. They correspond to two different mechanisms of strengthening meeting at a maximum for the transition between the two microstructures.

Acknowledgement

The authors thank Diplom. Ing G. Neuse, for making the Young's modulus measurements.

References

1. A. G. EVANS and G. TAPPIN, *Bull. Brit. Ceram. Soc.* **20** (1972) 275.
2. R. F. PABST, in "Fracture Mechanics of Ceramics", Vol. 2, edited by R. C. Bradt, D. P. H. Hasselman and F. F. Lange (Plenum Press, New York, 1974) p. 555.
3. R. W. RICE and S. W. FREIMAN, in 6th International Materials Symposium, University of California, Berkeley, August 1976.
4. R. W. RICE, K. R. McKINNEY, C. C. M. WU, S. W. FREIMAN and W. J. M. DONOUGH, *J. Mater. Sci.* **20** (1985) 1392.
5. R. T. DEHOFF and F. N. RHINES, "Quantitative Microscopy" (McGraw-Hill, New York, 1968).
6. J. SERRA, "Image analysis and mathematical morphology" (Academic Press, London, 1982, 1988).
7. M. COSTER and J. L. CHERMANT, "Précis d'analyse d'images" (Ed. du CNRS, 1989).
8. J. L. CHERMANT, M. COSTER and J. P. JERNOT, in "Modern developments in powder metallurgy", Vol. 12, edited by H. H. Hausner, H. W. Anteo and G. D. Smith (Plenum Press, New York, 1981) p. 377.
9. J. P. JERNOT and J. L. CHERMANT, *A.T.B. Metall.* **23** (1983) 13.
10. J. P. JERNOT, *Sci. tech. de l'armement* **59** (230) (1985) p. 283.
11. *Idem, Ann. Chim.* **10** (1985) 319.
12. G. VADAM, Thèse de Docteur Ingénieur, University of Caen (1978).
13. T. A. MICHALSKE, in "Fracture Mechanics of Ceramics", Vol. 5, edited by R. C. Bradt, A. G. Evans, D. P. H. Hasselman and F. F. Lange (Plenum Press, New York, 1983) p. 277.
14. J. K. MACKENZIE, *Proc. Phys. Soc.* **63B** (1950) 2.
15. R. MEYER and J. PILLOT, *Mem. Sci. Rev. Met.* **68** (1971) 695.
16. R. HAYNES, *Powd. Metall.* **14** (1971) 64.
17. J. P. JERNOT, *Mécan. Matér. Elect.* **415** (1986) 47.
18. M. EUDIER, *Powd. Metall.* **6** (1982) 278.
19. R. T. DE HOFF and J. P. GILLARD, in "Modern developments in Powder Metallurgy", Vol. 4, edited by H. H. Hausner (Plenum Press, New York, 1971) p. 281.
20. F. P. KNUDSEN, *J. Amer. Ceram. Soc.* **42** (1959) 376.
21. L. CORONEL, Thèse de l'Université de Caen (1989).
22. L. CORONEL and F. OSTERSTOCK, in "Euro-Ceramics", Vol. 3 (Elsevier Applied Science, 1989) edited by G. de With, R. A. Terpstra and R. Metselaar) p. 210.
23. T. TRAVERS, M. AMMI, D. BIDEAU, A. GERVOIS, J. C. MESSAGER and J. P. TROADEL, *Europhys. Lett.* **4** (1987) 329.

Received 13 June
and accepted 22 November 1989